

tion and the pore size, which allows one to prepare any desired pore size within the range of 15 to 35 nm.

Brunauer-Emmett-Teller surface areas, calculated from nitrogen adsorption isotherms, showed that the surface area of the silica templates was 80 m²/g, which decreased to 50 m²/g after the pellets were sintered. The DVB and EDMA polymer replicas had surface areas of 70 and 40 m²/g, respectively. The near coincidence in the surface areas of the template and of the porous polymers is consistent with the faithful replication of one surface from the other. The lower surface area of the EDMA replica arises from its shrinkage. Pore volume plots (Fig. 4B) show that the replicas have larger pores than the colloidal silica template, as is expected from the fact that the fraction of space filled in the former is about 75% (23).

The replication process was taken one step further by using the porous polymers as templates themselves in which to grow silica particles. Figure 3F shows a TEM image of silica particles 15 nm in diameter that were obtained from the 0.50 mole fraction EDMA replica. The polymer pellet was filled with a mixture of tetraethyl orthosilicate and aqueous ammonia. After the hydrolysis reaction was complete, the pellet was calcined in air at 450°C to remove the polymer. The spherical shape and long range order of the pores were not retained in this second generation replica. Nevertheless, it was possible to produce smaller silica particles from large ones through the replication/shrinkage cycle. A control experiment carried out without the porous polymer shows that much larger (200 to 1000 nm) polydisperse silica particles are produced in the absence of a template.

The colloidal silica templates can be prepared inexpensively on a scale of hundreds of grams, so this is a viable route to the production of bulk mesoporous materials. Additionally, silica template particles with diameters up to 70 nm can be made by the same method (22), and thus we anticipate that the replication method could cover an even larger range of pore sizes. The polymerization reaction can incorporate a wide variety of vinyl monomers (for example, we have prepared porous DVB- and EDMA-methacrylic acid copolymers in this way), and so the possibility exists that specific chemical functionality can be imparted to the pores in these materials.

References and Notes

- C. T. Kresge, M. E. Leonowicz, W. J. Roth, J. C. Vartuli, J. S. Beck, *Nature* **359**, 710 (1992).
- S. A. Bagshaw, E. Prouzet, T. J. Pinnavaia, *Science* **269**, 1242 (1995).
- D. Zhao, G. Huo, J. Feng, B. F. Chmelka, G. D. Stucky, *J. Am. Chem. Soc.* **120**, 6024 (1998).
- G. A. Ozin, *Acc. Chem. Res.* **30**, 17 (1997).
- O. D. Velev, T. A. Jede, R. F. Lobo, A. M. Lenhoff, *Nature* **389**, 447 (1997); A. Imhof and D. J. Pine, *ibid.*, p. 948; B. T. Holland, C. F. Blanford, A. Stein, *Science* **281**, 538 (1998); J. E. G. J. Wijnhoven and W. L. Vos, *ibid.*, p. 802.
- S. H. Park and Y. Xia, *Adv. Mater.* **10**, 1045 (1998).
- A. A. Zakhidov, et al., *Science* **282**, 897 (1998); A. van Blaaderen, *ibid.*, p. 887.
- Y. Xia and G. M. Whitesides, *Angew. Chem. Int. Ed. Engl.* **37**, 550 (1998).
- S. Y. Chou, P. R. Krauss, P. J. Renstrom, *Science* **272**, 85 (1996).
- P. E. Sokol, M. R. Gibbs, W. G. Stirling, R. T. Azuah, M. A. Adams, *Nature* **379**, 616 (1996); B. S. Schirato, M. P. Fang, P. E. Sokol, S. Komarneni, *Science* **267**, 369 (1995).
- C. B. Murray, C. R. Kagan, M. G. Bawendi, *Science* **270**, 1335 (1995).
- C.-G. Wu and T. Bein, *ibid.* **266**, 1013 (1994); *ibid.* **264**, 1757 (1994).
- F. Blatter and E. Schumacher, *Surf. Sci.* **203**, 571 (1988).
- T. J. Bandoz et al., *Chem. Mater.* **8**, 2023 (1996).
- T. Kyotani, N. Sonobe, A. Tomita, *Nature* **331**, 331 (1988); N. Sonobe, T. Kyotani, A. Tomita, *Carbon* **4**, 573 (1988); N. Sonobe, T. Kyotani, Y. Hishiyama, M. Shiraiishi, A. Tomita, *J. Phys. Chem.* **92**, 2, 7029 (1988); N. Sonobe, T. Kyotani, A. Tomita, *Carbon* **28**, 483 (1990); *ibid.* **29**, 9, 61 (1991); T. Kyotani, H. Yamada, N. Sonobe, A. Tomita, *ibid.* **32**, 2, 627 (1994); T. Kyotani, T. Mori, A. Tomita, *Chem. Mater.* **6**, 2138 (1994).
- H. Masuda and K. Fukuda, *Science* **268**, 1466 (1995).
- J. N. Weber, E. W. White, J. Liebig, *Nature* **233**, 337 (1971); R. L. White, J. N. Weber, E. W. White, *Science* **176**, 1922 (1972); D. M. Roy and S. K. Linnehan, *Nature* **247**, 220 (1974).
- C. R. Martin, *Science* **266**, 1961 (1994); *Acc. Chem. Res.* **28**, 8, 61 (1995); *Chem. Mater.* **8**, 1739 (1996); B. B. Lakshmi, P. K. Korhout, C. R. Martin, *ibid.* **9**, 857 (1997).
- S. A. Johnson, E. S. Brigham, P. J. Ollivier, T. E. Mallouk, *Chem. Mater.* **9**, 2448 (1997).
- S. A. Johnson, D. Khushalani, N. Coombs, T. E. Mallouk, G. A. Ozin, *J. Mat. Chem.* **8**, 1, 13 (1998).
- P. K. Dhal and F. H. Arnold, *J. Am. Chem. Soc.* **113**, 7417 (1991).
- Silica colloids were made by a slight modification of the technique described by K. Osseo-Asare and F. J. Arriagada [*Colloids Surf.* **50**, 321 (1990)]. A microemulsion was prepared by rapidly stirring 150 ml of cyclohexane, 6 ml of *n*-hexanol, 19 ml of Triton N-101, 7 ml of water, and 1.7 ml of 28% aqueous ammonia. To this was added 10 ml of tetraethyl orthosilicate, and the mixture was stirred at ambient temperature for 2 days. Most of the solvent was removed by rotary evaporation, and 100 ml of ethanol was added. The mixture was stirred for 1 hour, then centrifuged. The product solid was resuspended in ethanol and centrifuged three times, then dried at 80°C. TEM images showed that the particle diameter was 35 ± 2 nm. Tabular pellets (0.7 cm in diameter; thickness, 0.3 cm) were made from the dry powder by means of a pellet press.
- The pore size plots in Fig. 4B were calculated from adsorption isotherms with a model that is optimized for much smaller slit-shaped pores (24). The maxima are systematically shifted to pore diameters larger than are found by TEM (Figs. 1 through 3).
- J. P. Olivier, W. B. Conklin, M. Y. Szombathely, in *Characterization of Porous Solids. Proceedings of the IUPAC Symposium (COPS III)* (Elsevier, Marseille, France, 1993).
- This work was supported by grant GM-43844 from NIH. We thank R. Walsh and the Electron Microscope Facility for the Life Sciences in the Biotechnology Institute at Pennsylvania State University for the use of the TEM and S. Kumar, P. Sokol, and J. Patel for helpful discussions.

28 October 1998; accepted 4 January 1999

Dislocations Faster than the Speed of Sound

Peter Gumbsch¹ and Huajian Gao^{1,2}

It is thought that dislocations cannot surpass the sound barrier at the shear wave velocity because the energy spent in radiation has a singularity there. Atomistic simulations show that dislocations can move faster than the speed of sound if they are created as supersonic dislocations at a strong stress concentration and are subjected to high shear stresses. This behavior is important for the understanding of low-temperature deformation processes such as mechanical twinning and may be relevant for the dynamics of tectonic faults. The motion of the dislocations at a speed of $\sqrt{2}$ times the shear wave velocity can be understood from a linear elastic analysis, but many of the peculiarities of the supersonic dislocations are dominated by nonlinear effects that require a realistic atomistic description.

The irreversible plastic deformation of crystalline materials is mainly carried by the motion of dislocations, which are line defects of the crystal lattice. The velocity of these dislocations is limited by the lattice friction and by drag effects from the interaction with lattice vibrations and mobile electrons (*1*). At low temperatures and high stresses, dislocation velocities can reach sizeable fractions of the transverse acoustic wave velocity c_T .

Conventional wisdom, based on elasticity theory, is that dislocations cannot reach c_T because the energy required to drive a dislocation becomes infinite at this speed (*1*).

However, Eshelby noted that a singular radiation-free state exists for the motion of gliding edge dislocations at $\sqrt{2}c_T$ in an isotropic solid (*2*). Although this state is regarded as a mathematical curiosity rather than a physically relevant state of motion, it could in principle be accessible to dislocation motion if the dislocations could acquire this velocity. At all other velocities above c_T , elasticity theory shows that dislocations have negative energy release rates because they emit radiation (*1, 3*). Steady mo-

¹Max-Planck-Institut für Metallforschung, Seestrasse 92, 70174 Stuttgart, Germany. ²Department of Mechanical Engineering, Stanford University, Stanford, CA 94305, USA.

REPORTS

tion at these velocities is possible only if energy is continuously provided by an applied stress or by atomic readjustment in the glide plane (4, 5). Above c_T but below the longitudinal wave velocity c_L , in the so-called transonic velocity regime, the radiation should form one symmetrical pair of shock fronts of shear wave character, comparable to a Mach cone. In the supersonic regime (above c_L), two pairs of shock fronts of longitudinal and shear wave character are predicted for the linear elastic isotropic solid (3).

In elasticity theory, a dislocation and a crack are both described as stress singularities of different strength. Analogous to dislocation motion, a singular radiation-free transonic state also exists for the motion of shear cracks. The radiation-free solution for cracks occurs at the same velocity as that for dislocations for any anisotropic elastic solid (6). Although experimentally determined dislocation velocities have all been lower than c_T , transonic shear cracks have been observed in high-speed impacts (7). Tectonic shear faults have also been reported to move at velocities above c_T (8).

To study transonic and supersonic dislocations by atomistic simulations, one cannot start with a subsonic dislocation and accelerate it, because it cannot get through the sound barrier at c_T (9). However, one can try to directly create transonic dislocations and study their properties.

In our simulations, a thin strip was subjected to homogeneous simple shear ϵ (Fig. 1). Analogous to the strip geometry used for dynamic fracture studies (10), the long sides were clamped, and periodic boundary conditions of minimal length were applied in the third direction. The short sides were left free, except for the left upper half, which was moved to the right at a constant velocity (up to 65 m/s) to mimic an indenter with a sharp edge. This edge locally raised the stress very efficiently, resulting in the creation of a dislocation at the point of indentation.

The elastically isotropic material tungsten was chosen as our model material, and the Finnis-Sinclair potential (11, 12) was used to model the atomic interactions. A $\langle 111 \rangle$ direction was aligned with the long axis of the strip so that the indentation process produced edge dislocations on a $\{2\bar{1}1\}$ plane characterized by a displacement discontinuity (Burgers vector) $b = a_0/2 \langle 111 \rangle$, where a_0 denotes the lattice parameter. These are natural dislocations of the body-centered cubic lattice of tungsten. Shear was applied in the antitwinning direction. The motions of all atoms were followed in a microcanonical molecular dynamics simulation at a time step of $\Delta t = 2$ fs. The length of the time step and the indentation speed were varied independently to ensure that neither the velocity of the dislocation nor any other relevant quantity was influenced substantially. The simulations were started at a low initial temperature of

10 K. This temperature rose to between 30 and 70 K while the dislocation passed through the strip.

After injection, the dislocations quickly reached an almost constant velocity, at which they moved through most of the specimen. The average velocity \bar{v} was determined over the central section of the specimen and was plotted as a function of the applied strain ϵ (Fig. 2), together with the relevant wave velocities.

At a low applied strain, the dislocations moved subsonically with an average velocity of $0.65c_T$ to $0.7c_T$. At intermediate applied strains, they started transonically but then dropped below c_T and continued to move subsonically. This drop below the sound barrier was not continuous; the dislocation moved with decreasing transonic velocity and then suddenly stopped and rested for ~ 0.5 ps at the same position. The wide core of the transonic dislocation contracted during this arrest period to the size of the subsonic dislocation (Fig. 3). Just before stopping, the shock wave of the transverse acoustic waves was clearly visible (Fig. 3A); 0.6 ps after stopping, the center of the dislocation had not moved, but the core had contracted, and the radiation wave had passed the dislocation (Fig. 3B). After this arrest period, the dislocation moved subsonically at a velocity of $\sim 0.7c_T$.

Higher enforced strains resulted in a stable transonic dislocation motion at a velocity increasing from $1.38c_T$ to $1.5c_T$ with increasing applied strain. The flat and extended dislocation core of a transonic dislocation moving at $\sim 1.4c_T$ is shown in Fig. 3C. The velocity distribution clearly shows a well-developed shock wave from the transverse acoustic waves on the lower, dilatational side of the dislocation. Nothing comparable is seen on the upper, compressive side.

Increasing the applied strain even further

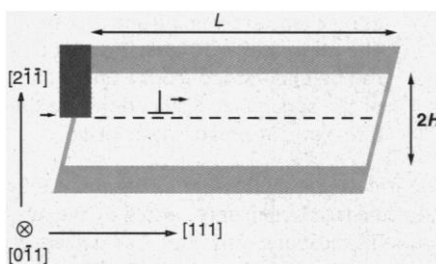


Fig. 1. Schematic outline of the strip geometry used for the atomistic simulation of dislocation motion. The strip is clamped in the upper and lower surface regions and homogeneously sheared. An indenter with a sharp edge is pushed into the surface of the left side to create the dislocation that then moves along the strip. The dislocation is indicated by \perp ; the viewing direction is indicated by \otimes . Small arrows show the direction of motion of the indenter and of the dislocation. The aspect ratio H/L is $1/5$, where $2H$ is the height of the atomistic model and the length L represents 100 lattice parameters.

eventually allowed the dislocation to surpass the velocity of longitudinal sound waves as well. The core configuration (Fig. 3D) was not very different from the core of the transonic dislocation (Fig. 3C), but the shock waves trailing the dislocations showed an even more pronounced anisotropy with respect to the $\{211\}$ glide plane. The longitudinal waves produced one well-developed shock front below the glide plane. Above the glide plane, a series of four to five very severe and localized shock fronts was observed. All of them were compressive in character.

These results are surprising in several aspects. First, the observation of transonic dislocation motion in atomistic simulations is surprising because subsonic dislocations should not be able to surmount the sound barrier at c_T . Second, given a transonic dislocation, it is surprising that it can exist in a relatively wide velocity corridor of $1.3c_T$ to $1.6c_T$. Third, dislocation motion above the longitudinal wave speed has hitherto not been considered possible.

Although it was known that linear elasticity theory allows dislocation motion above the shear wave velocity (1, 2, 4), it was thought (1, 13) and even demonstrated in atomistic simulations (9) that dislocations could never reach that speed. However, it was observed in our atomistic simulations that the dislocation does not surmount the sound barrier at c_T but is already "born" with transonic velocity. The stress concentration at the sharp indenter edge appears sufficiently high to immediately push the dislocation above c_T . Analyzing the nucleation process in detail in the atomistic simulations does not reveal any subsonic motion before the transonic stage. Even the dislocations that later move subsonically seem to be created

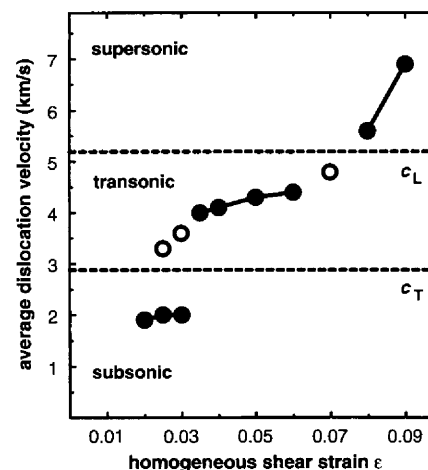


Fig. 2. Average dislocation velocity versus applied shear strain. The different regimes of stable dislocation motion at constant velocity (solid circles) are connected by solid lines. Open circles mark substantially varying velocities or the (average) velocity of dislocations before stopping. Dashed lines indicate the relevant acoustic wave velocities.

REPORTS

at a very high speed, mutating to slower speeds shortly after nucleation. The nucleation of transonic dislocations therefore appears to be dominated by the stress concentration at the indenter edge rather than by the absolute values of the applied stress or strain. In contrast, a critical strain appears to be necessary to maintain a dislocation at the transonic speed. Whereas linear elastic continuum theory predicts a radiation-free state at a velocity of $\sqrt{2}c_T$, which would not require any driving force, the dislocations in our simulations always radiate strongly, even if they are traveling exactly at $\sqrt{2}c_T$, as in Fig. 3C. The energy radiated can only be drawn from the applied strain field.

In studies that address the issue of dislocation motion above c_T [for example, (1, 3)], it is sometimes argued that the energy could only come from the plane of motion, which would require that the moving dislocation eliminates some high-energy fault during its motion. However, it can easily be shown that the applied stress is doing work on the dislocation and yields an effective driving force no

matter how fast it moves (5).

Extending Weertman's analysis of a transonic Peierls dislocation (3) to the case of an applied strain field, we found that the energy G_d released per unit distance of dislocation motion for the transonic dislocation can be calculated from the formula given in (3)

$$G_d = \int_{-\infty}^{\infty} \sigma(x)B(x) dx \quad (1)$$

where $B(x)$ is the Burgers vector distribution and $\sigma(x)$ is the shear stress along the glide plane of the dislocation. Adding an applied stress σ^{app} to the intrinsic stress field of the dislocation $\sigma^{\text{disl}}(x)$ given in (3), one obtains

$$G_d = \sigma^{\text{app}}b - A(v) \int_{-\infty}^{\infty} [B(x)]^2 dx \quad (2)$$

where the prefactor $A(v)$ is dependent on the velocity v of the dislocation (Fig. 4). A

similar analysis is given in (5). In Eq. 2, $\sigma^{\text{app}}b$ is the familiar Peach-Koehler force on a dislocation, and

$$A(v) \int_{-\infty}^{\infty} [B(x)]^2 dx$$

describes the energy radiated from the dislocation. For a dislocation to propagate at a particular transonic speed, the driving force must be positive ($G_d > 0$). Because $A(v)$ is always greater than or equal to zero, the radiation always exerts a negative driving force and provides a drag on dislocation motion. The work done by the applied stress must be sufficiently large to overcome this resistance.

Linear elasticity thus predicts vanishing radiation at a velocity of $\sqrt{2}c_T$, and accordingly, nonlinearities in the core region must be responsible for the leaking of energy through radiation. This leakage must be supplied from the Peach-Koehler term and therefore requires a finite applied stress for transonic motion (as seen in Fig. 2).

From this linear elastic analysis, it is clear that the velocity of $\sqrt{2}c_T$ is attractive for the dislocation because the linear elastic fields can be radiation-free at this velocity. Any other velocity will have an additional radiative elastic part and therefore require higher driving forces. For strains higher than the critical strain, this results in slightly increasing dislocation velocities. For lower strains, this elastic radiation retards the dislocation until it drops out of the transonic regime, because $A(v)$ (and, concomitantly, the elastic energy release rate per unit advance of the dislocation) diverges at c_T (Fig. 4). In accord with a diverging energy release rate, the atomistic simulations at lower than

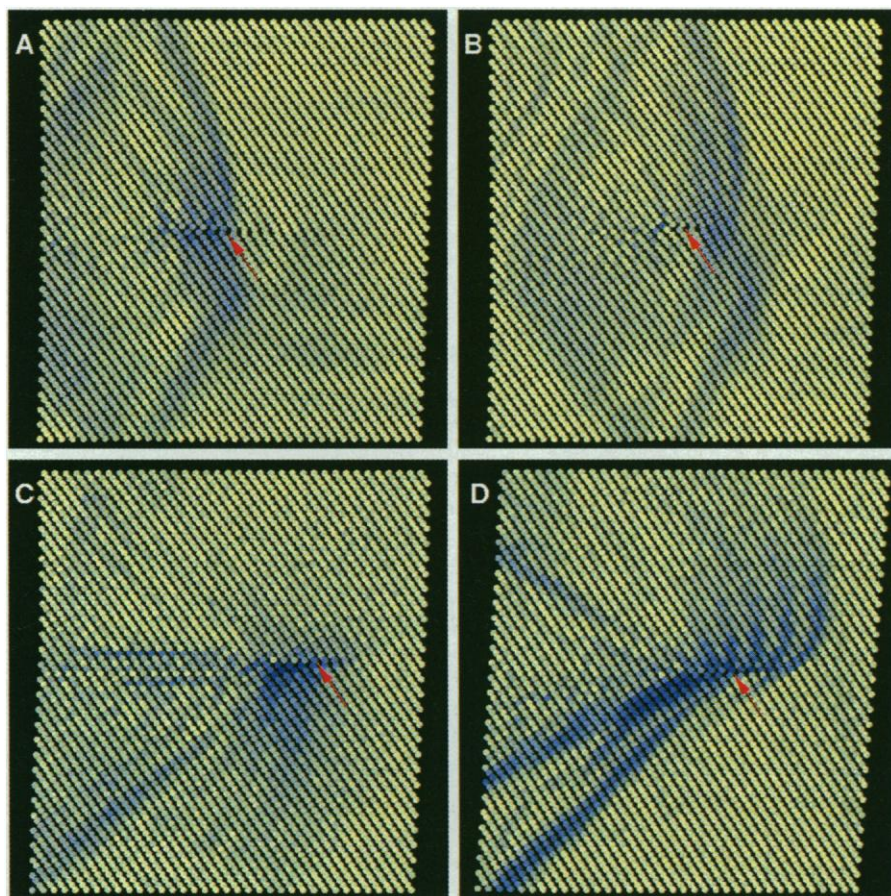


Fig. 3. Snapshots of the atomic configuration of small regions around moving dislocations. The dislocations move from the left to the right. The blue color indicates the magnitude of the in-plane velocity. Areas of dark blue denote atoms that are moving faster than 500 m/s. Red arrows indicate the centers of the dislocations. The discontinuous displacement introduced into the crystal lattice by the dislocation can best be viewed from the direction indicated by the arrows. The stopping dislocation at an applied strain of $\varepsilon = 0.03$ is shown (A) just before stopping and (B) 0.6 ps later, as it starts moving again subsonically. (C) A transonic dislocation moving steadily at a velocity of $\sim 1.4c_T$; (D) a supersonic dislocation at an applied strain of $\varepsilon = 0.08$.

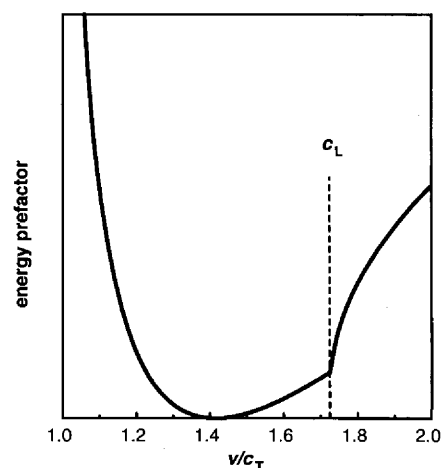


Fig. 4. Schematic drawing of the linear elastic solution for the velocity dependence of the energy spent in radiation, which is characterized by the prefactor $A(v)$ of Eq. 2. At the velocity $v = \sqrt{2}c_T$, the prefactor $A(v)$ becomes zero and the radiation vanishes. Quantitatively, $A(v)$ depends on details of the shape of the dislocation core.

critical strains show that the dislocation stops before it starts to move again subsonically.

The observed transition to the supersonic state and the greater increase of dislocation velocity in the supersonic regime cannot be understood from the linear elastic analysis because $A(v)$ monotonically increases with the velocity of the dislocation above $\sqrt{2}c_T$ (Fig. 4). The second sound barrier at c_L therefore must be entirely caused by the nonlinearity and the finite range of the atomic interaction in the dislocation core region. This is displayed by the asymmetry of the longitudinal shock waves emanating from the supersonic dislocation (Fig. 3D). Linear elasticity would predict one symmetrical pair of shock fronts, whereas the atomistic simulations show a much richer distribution. The upper, compressive part of the dislocation produces a series of very severe shock fronts, whereas the lower side develops only one front. Whether this asymmetry has its origin in the sign of the stress field of the dislocation or whether it is a result of crystal orientation cannot be decided from the present calculations alone.

Comparing the atomistic simulations in a finite thin strip with continuum elasticity theory for an infinite sample and attributing some of the observed features to nonlinearities is of course questionable as long as one has not investigated size effects in the atomistic model. To do so, we repeated the calculations for a model in which all lengths were changed by a factor of 2 for the case of an externally applied strain of $\varepsilon = 0.05$. Whereas the smaller system gives a 10% slower dislocation, the large system is almost indistinguishable from the system used so far in both the dislocation velocity and the distribution of the atomic velocities around the dislocation core (compare Fig. 3C). Although these results, of course, do not constitute a proper system-size scaling analysis, they give confidence that the conclusions drawn so far are not critically dependent on system size.

The practical importance of these transonic and supersonic dislocations appears to be limited by the difficulty of nucleation and by the high stresses that are required for sustained motion at these high velocities. From the discussion of the nucleation conditions, it has been concluded that an intense stress concentration is required for the nucleation of transonic dislocations. Stress concentrators with an efficiency similar to that of the sharp indenter could either be a dislocation pileup at a strong obstacle or a crack, which is characterized by a stress singularity at its tip. Conditions that give the extremely high background stresses required for continuous long-distance propagation at the transonic or supersonic speed are present in low-temperature deformation, where thermally activated deformation processes are suppressed. In addition to the motion of individual dislocations, deformation at low temperatures is often

carried by mechanical twinning, which can be viewed as the concerted motion of several partial (twinning) dislocations. Consequently, one may also regard low-temperature mechanical twinning as a case where transonic motion could be observable. The motion of mechanical twins above c_T has indeed been predicted for applied stresses (or strains) above a critical value in an analytical nonlinear elasticity study (14). Using high-speed photography, Finkel' (15) has documented that the first thin twins formed in dynamically loaded steel sheets propagate at velocities of $0.80c_L$ to $0.85c_L$, corresponding almost exactly to the transonic velocity regime observed here. In later stages of the deformation, twins were observed to move at velocities of $0.40c_L$ to $0.45c_L$, corresponding to the subsonic regime in Fig. 2.

Whether supersonic dislocations may be relevant for geophysical phenomena is as yet unclear. On the one hand, the increasing temperature in the deeper crust makes thermally activated processes more likely; on the other hand, low-symmetry crystal structures and the limited amount of slip systems certainly allow the buildup of large stresses, which may reach the required order of magnitude.

Future work should focus on the nucleation conditions that result in supersonic dislocations. Supersonic dislocations may help to understand some of the deformation phenomena that are usually considered collective, and therefore, the dynamics of mechanical twinning, martensitic transforma-

tion, and tectonic shear faults may have to be reinvestigated while considering the results presented here.

References and Notes

1. J. P. Hirth and J. Lothe, *Theory of Dislocations* (Wiley, New York, 1982).
2. J. D. Eshelby, *Proc. R. Soc. London A* **62**, 307 (1949).
3. J. Weertman, in *Mathematical Theory of Dislocations*, T. Mura, Ed. (American Society of Mechanical Engineers, New York, 1969), pp. 178–202.
4. F. R. N. Nabarro, *Theory of Crystal Dislocations* (Oxford Univ. Press, Oxford, 1967).
5. J. Weertman and J. R. Weertman, in *Dislocations in Solids*, F. R. N. Nabarro, Ed. (North-Holland, Amsterdam, 1980), vol. 3, pp. 1–60.
6. H. Gao, Y. Huang, P. Gumbsch, A. J. Rosakis, *J. Mech. Phys. Solids*, in press.
7. A. J. Rosakis, D. Coker, O. Samundrala, *Caltech SM Rep. 98-17* (California Institute of Technology, Pasadena, 1998).
8. R. J. Archuleta, *Bull. Seismol. Soc. Am.* **72**, 1927 (1982).
9. J. Schiotz, K. W. Jacobsen, O. H. Nielsen, *Philos. Mag. Lett.* **72**, 245 (1995).
10. P. Gumbsch, *Z. Metallkd.* **87**, 341 (1996).
11. M. W. Finnis and J. E. Sinclair, *Philos. Mag. A* **50**, 45 (1984).
12. G. J. Ackland and R. Thetford, *ibid.* **56**, 15 (1987).
13. J. Friedel, *Dislocations* (Pergamon, Oxford, 1964).
14. P. Rosakis and H. Tsai, *Int. J. Solids Struct.* **32**, 2711 (1995).
15. V. M. Finkel', I. N. Voronov, A. M. Savel'Yev, A. I. Yeliseyenko, V. A. Fedorov, *Fiz. Met. Metalloved.* **29**, 1248 (1970).
16. Inspiring discussions with R. Phillips, Brown University, on the nucleation of supersonic dislocations as well as his suggestion of the indenter geometry are gratefully acknowledged. H.G. would like to thank the Alexander von Humboldt foundation for financial support of his stay at the Max-Planck-Institut für Metallforschung in Stuttgart.

21 September 1998; accepted 6 January 1999

Chemical Analysis of Polar Stratospheric Cloud Particles

Jochen Schreiner,¹ Christiane Voigt,¹ Andreas Kohlmann,¹ Frank Arnold,¹ Konrad Mauersberger,^{1*} Niels Larsen²

A balloon-borne gondola carrying a particle analysis system, a backscatter sonde, and pressure and temperature sensors was launched from Kiruna, Sweden, on 25 January 1998. Measurements within polar stratospheric cloud layers inside the Arctic polar vortex show a close correlation between large backscatter ratios and enhanced particle-related water and nitric acid signals at low temperatures. Periodic structures in the data indicate the presence of lee waves. The H_2O/HNO_3 molar ratios are consistently found to be above 10 at atmospheric temperatures between 189 and 192 kelvin. Such high ratios indicate ternary solution particles of H_2O , HNO_3 , and H_2SO_4 rather than the presence of solid hydrates.

The important role of polar stratospheric clouds (PSCs) during the development of the south polar ozone hole was recognized soon

after the first publication (1) on large unexpected ozone losses in the lower stratosphere over Antarctica. Initially, the existence of cloud particles at temperatures above the ice point was puzzling; however, thermodynamic considerations (2) as well as laboratory studies (3) revealed that in the H_2O-HNO_3 system stable crystalline hydrates can be formed above the ice point. During the last 10 years the initial concept of two types of PSCs—

¹Max-Planck-Institut für Kernphysik, Division of Atmospheric Physics, Post Office Box 103 980, D-69029 Heidelberg, Germany. ²Danish Meteorological Institute, Division of Middle Atmosphere Research, Lyngbyvej 100, DK-2100 Copenhagen, Denmark.

*To whom correspondence should be addressed.